Nonlinear Fast Modeling Method of Flux Linkage and Torque for a 12/8 Switched Reluctance Motors

Xiaodong Sun, *Senior Member, IEEE*, Nuonuo Wang, Yunfei Cao, Dong Guo, Ming Yao, Yueping Sun, and Yefei Xiong

***Abstract*—This article presents a nonlinear modeling method for the flux linkage and torque of a switched reluctance motor. The method is based on universal weighted least squares support vector machine regression (WLSSVR), combined with entropy method (EM) and improved coyote optimization algorithm (COA) to optimize the kernel parameters. Among them, EM can well improve the error of the general WLSSVR in the selection of sample weights, and the improved COA can prevent the system from falling into local optimum and improve the iteration speed. This SRM modeling method, which combines WLSSVR based on entropy and improved COA, can improve the modeling speed on the premise of ensuring the modeling accuracy mode speed. Finally, the effectiveness of the algorithm is verified by experiments.**

***Index Terms*—Coyote optimization algorithm, nonlinear modeling, switched reluctance motor, weighted least squares support vector machine regression.**

NOMENCLATURE

SRM	Switched reluctance motor.
WLSSVR	Weighted least squares support vector regression.
EM	Entropy Method.
COA	Coyote optimization algorithm.
EV	Electric vehicle.
HEV	Hybrid electric vehicle.
FEA	Finite element analysis.
BPNN	Back propagation neural network.
RBFNN	Radial basis function neural network.
RBFN-AFS	Radial basis function network.
SVR	Support vector machine regression.
LSSVR	Least square support vector machine regression.
BVC-RBF	Radial basis function neural network with boundary value constraints.
GA	Genetic algorithm.
PSO	Particle swarm optimization.
GWO	Gray wolf optimization algorithm.
BP-MTN	Multidimensional Taylor network based on backpropagation.
DTC	Direct torque control.
TSF	Torque sharing function.
EM-WLSSVR	Weighted least squares support vector regression.
MAE	Mean absolute error.
RMSE	Root mean square error.
SD	Standard deviation.
ω_R	Speed fluctuation.
T_{RM}	Torque ripple.

Manuscript received 11 June 2023; revised 12 October 2023 and 29 December 2023; accepted 1 February 2024. Date of publication 6 February 2024; date of current version 20 March 2024. This work was supported in part by the National Natural Science Foundation of China under Grant 62173162, in part by the Key Research and Development Program of Jiangsu Province under Grant BE2023052, in part by the Opening Foundation of International Joint Laboratory of Intelligent Manufacturing and Control of Key Parts for Energy-Efficient and New Energy Vehicles, Ministry of Education under Grant 2023IJLIMC04, and in part by the Opening Foundation of Key Laboratory of Advanced Manufacture Technology for Automobile Parts, Ministry of Education under Grant 2022 KLMT02. Recommended for publication by Associate Editor R. Kennel. *(Corresponding author: Ming Yao.)*

Xiaodong Sun, Nuonuo Wang, Yunfei Cao, and Yefei Xiong are with the Automotive Engineering Research Institute, Jiangsu University, Zhenjiang 212013, China (e-mail: xdsun@ujs.edu.cn; 2222204045@stmail.ujs.edu.cn; 2212104017@stmail.ujs.edu.cn; 2222004056@stmail.ujs.edu.cn).

Dong Guo is with the International Joint Laboratory of Intelligent Manufacturing and Control of Key Parts for Energy-Efficient and New Energy Vehicles, Ministry of Education, School of Vehicle Engineering, Chongqing University of Technology, Chongqing 400054, China (e-mail: guodong@cqut.edu.cn).

Ming Yao is with the School of Automotive and Traffic Engineering, Jiangsu university, Zhenjiang 212013, China (e-mail: ymluck@ujs.edu.cn).

Yueping Sun is with the School of Electrical and Information Engineering, Jiangsu university, Zhenjiang 212013, China (e-mail: sunypujs@ujs.edu.cn).

Color versions of one or more figures in this article are available at https://doi.org/10.1109/TPEL.2024.3363027.

Digital Object Identifier 10.1109/TPEL.2024.3363027

I. INTRODUCTION

A. Motivation

AS ENVIRONMENTAL pollution becomes more and more serious, research on electric vehicle (EV) and hybrid electric vehicle (HEV) has become more and more popular [1], [2], [3]. Therefore, as the core original components of EVs and HEVs, the research on drive motors has received more and more attention. At present, the mainstream drive motors are often composed of permanent magnet synchronous motor (PMSM) [4], [5], [6]. However, PMSM are more expensive because they contain permanent magnets. And permanent magnets are prone to irreversible demagnetization under high-temperature conditions, which will reduce the efficiency of the motor.

Switched reluctance motor (SRM) can well overcome the above problems. SRM have a large starting torque, there is no permanent magnet, and each phase is independent, so it is cheap and has good fault tolerance [7], [8], [9], [10]. In SRM sensorless control, perturbations such as parameter adaptation and mutual coupling will produce flux linkage errors. Xiao et al. [9] used the augmented state observer and small signal approximation

model, the transient performance of the rotor was improved, and the estimation accuracy of the rotor position and speed was increased.

However, its inherent double salient structure leads to the highly nonlinear characteristics of its magnetic and torque characteristics [11], [12]. Therefore, it is difficult to derive its comprehensive mathematical model, which increases the difficulty of its control. Its high torque ripple characteristics also limit its wide application in EV and HEV [13], [14]. Therefore, the study of nonlinear modeling of the flux linkage and torque of SRM is of great research significance.

B. Related Research

In the research process of nonlinear modeling of SRM, the finite element analysis (FEA) [15], [16], [17] is the most used. The biggest advantage of this method is its high accuracy, but the higher the accuracy, the longer the calculation time, so it is not a highly implementable solution. In addition, analytical modeling methods are also used to model SRM. In [18], a model of magnetic equivalent circuits is proposed to facilitate the calculation of flux linkage and torque. In [19], a modeling method using the fourth-order Fourier series and Kriging model was proposed to better describe the flux linkage and torque characteristics. These two methods do not require FEA data, but the analytical model is quite complex and the accuracy is difficult to guarantee.

In [20], the method of constructing the SRM rotor position model through actual measurement and then using the improved algorithm of Back propagation neural network (BPNN) and radial basis function neural network (RBFNN) [21] was proposed, which can accurately predict the rotor position. In [22], an adaptive fuzzy system based on a radial basis function network (RBFN-AFS) is modeled as a 6/4-pole SRM, and the sample data for training and learning is obtained by experimental measurement. All of them can achieve higher accuracy. A new radial basis function neural network with boundary value constraints is proposed in [23] to calculate the flux linkage data. An improved multidimensional Taylor network architecture based on error backpropagation algorithm is proposed in [24]. However, there are many control parameters based on these methods, and a large number of thresholds and weights need to be updated each time, so the convergence speed will be too slow. If you want to improve the accuracy, you need to increase the number of hidden layers, which will greatly increase the research cost. Therefore, the practicality of these methods is not high.

Support vector machine regression (SVR) is a small-sample learning method, which can avoid the overfitting problem of general algorithms [25], so it is more suitable for dealing with the nonlinear modeling problem of flux linkage and torque of SRM. The general SVR is difficult to solve the problem of multiclassification. Therefore, in the nonlinear modeling of SRM, the least square support vector machine regression (LSSVR) is often used to replace the general SVR [26]. To enhance the anti-interference ability of LSSVR against abnormal points, a weighted least squares support vector machine regression (WLSSVR) was proposed. WLSSVR assigns different weights according to different training samples, which can alleviate the robustness of LSSVR during complex calculations. The accuracy and real-time performance of the model are guaranteed by selecting suitable activation function and polynomial order. Chen et al. [27] proposed a polynomial, which takes into account the error percentage correction coefficient to quickly and accurately build the flux linkage and torque model, which greatly reduces the time of multiobjective optimization process. Mihic et al. [28] presented a new analytical model which takes into account the mutual coupling effects between two or more simultaneously excited phases and reduce the number of input parameters.

Whether it is LSSVR or WLSSVR, the core parameters have a high impact on the performance of the algorithm, so the WLSSVR algorithm needs to be combined with an optimization algorithm. Currently, the more commonly used algorithms include genetic algorithm (GA) [29], particle swarm optimization (PSO) [30], [31], gray wolf optimization algorithm (GWO) [32], [33], and coyote optimization algorithm (COA).

Among these more commonly used algorithms, GA cannot use the feedback information of the network in time. The local search ability of PSO is poor, and it is easy to fall into the local extreme value. GWO has shortcomings such as low convergence accuracy and insufficient convergence speed. COA has a unique algorithm structure, which provides a new mechanism for the balance of exploration and development in the optimization process.

Direct torque control (DTC) [34] and torque sharing function (TSF) [35] are the most commonly used torque control methods used in SRM control. DTC and TSF are also often used for algorithm or model verification of SRM [36], [37]. The principles of the two are essentially different, but both can play a good role in suppressing torque ripple [38].

C. Contributions

In this article, an entropy method (EM) based on the improved coyote algorithm, WLSSVR, is proposed for the nonlinear modeling of SRM flux linkage and torque. Compared with the existing BPNN, RBFNN, and RBFN-AFS, EM-WLSSVR can improve the modeling speed while ensuring the modeling accuracy. When high modeling accuracy is required, EM-WLSSVR does not need a long time to complete the entire nonlinear modeling. The main contributions of this article are as follows.

1) Since the weights brought by the general WLSSVR are linearly distributed, there is a certain error in the selection of samples. In order to reduce the error in sample selection of WLSSVR, the regression model was optimized with EM.
2) The improved COA is used to optimize the neural network. Through the introduction of Wolf pack, the iteration rate of adult wolf will be greatly improved, and the local optimal situation can be effectively alleviated.
3) The EM-WLSSVR proposed in this article establishes a complete SRM nonlinear modeling system, and retains the application of FEA in SRM, which can ensure the basic modeling accuracy. And the new modeling method

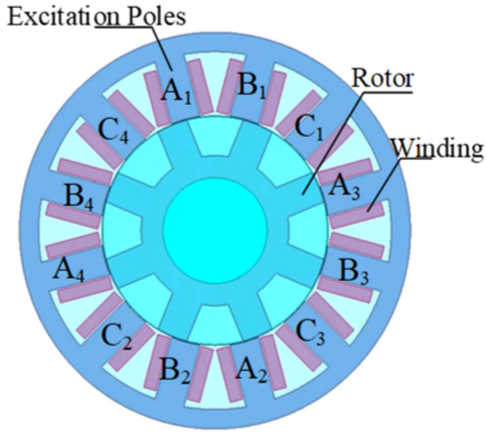

Fig. 1. Topology of 3-phase 12/8 SRM.

can replace the parameter table in SRM, so it has a high application value.

D. Article Organization

The rest of this article is organized as follows. Section II describes the basic mathematical models and FEA principles of SRM, and explains the shortcomings of FEA. Section III shows the mathematical models of the traditional WLSSVR and the improved EM-WLSSVR and clarifies their advantages. Section IV shows the mathematical models of traditional COA and improved COA and clarifies their advantages. Section V combines improved COA and EM-WLSSVR and simulates to verify their superiority, combines nonlinear modeling with DTC and TSF control systems commonly used in SRM, and verifies the accuracy and effectiveness of the proposed nonlinear modeling method through experiments. Finally, Section VI concludes this article.

II. Characteristics of Three-Phase 12/8 SRM

A. Structural Characteristics of 12/8 SRM

There are 12 stator poles in a 12/8 SRM, including 12 excitation poles. The excitation pole is full of windings. This structure is essentially formed by overlapping two 6/4 structures. This structure is a short magnetic circuit structure. The adjacent stator poles and the two opposite stator poles are energized at the same time, and the current is closed when the current passes through the other stator pole. This structure provides a buffer when the motor is commutated and reduces the torque dead zone. Fig. 1. illustrates the topology of a 3-phase 12/8 SRM.

B. Mathematical Model of SRM

First of all, the voltage balance equation of the phase voltage is obtained from the basic theorem of the circuit

$$U_k = R_k i_k - e_k = R_k i_k + \frac{d\psi_k}{dt}. \tag{1}$$

Among them, U_k, R_k, i_k, e_k, and ψ_k represent phase voltage, phase resistance, phase current, induced electromotive force, and winding flux, respectively. Among them, the flux linkage ψ_k can be expressed as a function of the current i and the rotor angle θ

$$\psi_k(i_k, \theta) = L_k(i_k, \theta) \cdot i_k. \tag{2}$$

When ignoring the mutual inductance between windings, the mechanical energy output by each phase of the SRM in one cycle is $W_k = \oint id\psi$. Based on the principle of virtual displacement, the instantaneous electromagnetic torque at any point can be expressed as

$$T_{mx} = -\frac{\partial W}{\partial \theta}\bigg|_{\psi=const} = \frac{\partial W'}{\partial \theta}\bigg|_{i=const}. \tag{3}$$

In the formula, W is the energy storage of the winding, $W = \int_0^{\psi} i(\psi, \theta)\, d\psi$. W' is the coenergy of the winding, $W' = \int_0^{i} \psi(i, \theta)\, di$.

Finally, the entire working range of the SRM is integrated, and the expression of the average output electromagnetic torque is obtained

$$T_e = \frac{mN_r}{2\pi} \int_0^{2\pi/N_r} T_{mx}(\theta, i) d\theta. \tag{4}$$

Theoretically, the value of electromagnetic torque can be directly calculated by the formula (3), but the instantaneous torque T_{mx} of SRM is a highly nonlinear value, and there is no accurate expression to describe its relationship with rotation angle θ and phase current i, neither the SRM's flux linkage ψ_k.

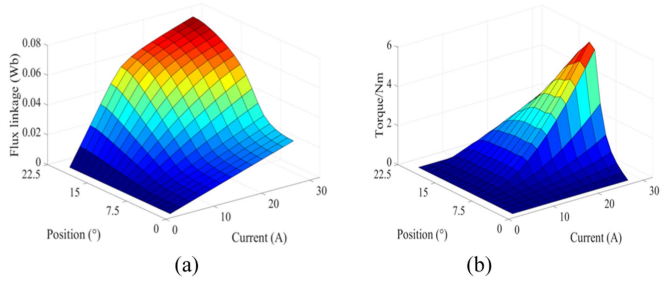

(a) (b)

Fig. 2. Two-dimensional curve group of FEA results. (a) Flux linkage. (b) Torque.

C. Application of FEA in SRM Modeling

FEA is a numerical calculation method for solving the approximate value of the true solution of partial differential equations. Therefore, FEA is often used to analyze the mathematical relationship between current-angle-flux [i−θ−Ψ] and current-angle-torque [i−θ−T]. The relationship data of magnetic flux and torque with current and rotor position angle are obtained by the following method. The data of the rotor position angle is obtained through finite element analysis and stored in the form of a table. Then, the conversion from magnetic flux and rotor position angle to current is realized by a nonlinear interpolation algorithm. In the same way, the conversion from current and rotor position angle to current and the conversion from current and rotor position angle to torque can also be achieved by nonlinear interpolation. Fig. 2. illustrates the two-dimensional (2-D) curve group of flux linkage and torque results under FEA.

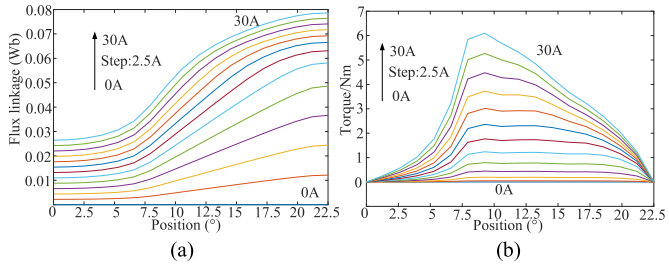

(a) (b)

Fig. 3. Three-dimensional distribution diagram of FEA results. (a) Flux linkage. (b) Torque.

Fig. 3 illustrates the 3-D distribution diagram of flux linkage and torque results under FEA.

However, the look-up table data produced by the FEA method is discretely distributed, which means that the look-up table method cannot achieve very high accuracy. If you want to improve the accuracy, you must shorten the sampling interval of current and angle, but this will greatly increase the amount of data, which will increase the cost of research. Therefore, FEA is not the optimal solution.

III. SRM Nonlinear Modeling Based on EM-WLSSVR

A. Basic Principles of WLSSVR

First, the training sample set $(x_i, y_i)|i = 12,3, \ldots, n$, is established. Among them, x_i is an n-dimensional input variable, and y_i is an output variable, where $x_i \in R^n$ and $y_i \in R$.

Therefore, the regression model is established

$$f(x) = \omega^T \cdot \phi(x) + b \tag{5}$$

where the $\phi(x)$ is the spatial mapping function, ω is the weight vector matrix, and b is the deviation vector. As long as there is an input variable x_i, the output value y_i can be obtained through the regression function.

Then, the standardized cost function of LSSVR can be expressed as

$$\begin{cases} \min J(\omega, \xi) = \frac{1}{2}\|\omega\|^2 + \frac{C}{2}\sum_{i=1}^{n}\sigma_i\xi_i^2 \\ \text{s.t.} \;\; y_i = \omega^T \cdot \phi(x_i) + b + \xi_i, i = 1, 2, 3, \ldots, n. \end{cases} \tag{6}$$

Among them, C is a regularization parameter, which is often used to balance the empirical error of the model, σ_i is the weight, and ξ_i is the fitting error.

To find the optimal solution of the function, (6) is transformed into the form of the Lagrange equation

$$L(\omega, \xi, \alpha, b) = J(\omega, \xi) - \sum_{i=1}^{n}\alpha_i(\omega^T \cdot \phi(x_i) + b + \xi_i - y_i). \tag{7}$$

In (7), α_i is the Lagrangian multiplier. According to Karush–Kuhn–Tucker conditions, it can be obtained

$$\begin{pmatrix} 0 & e^T \\ e & K + C^{-1}U \end{pmatrix} \begin{pmatrix} b \\ \alpha^* \end{pmatrix} = \begin{pmatrix} 0 \\ y \end{pmatrix}. \tag{8}$$

In (8): K is the kernel matrix, I is the identity matrix, and y is the set of output vectors. The specific expression of each parameter is

$$\begin{cases} K = K_{ij} = \phi(x_i)^T\phi(x_j) = K(x_i, x_j) \\ y = (y_1, y_2, y_3, \ldots, y_n)^T \\ e = (1, 1, 1, \ldots, 1)^T. \end{cases} \tag{9}$$

According to (8) and (9), α_i^* and b can be solved. Therefore, another regression expression of LSSVR can be obtained

$$f(x) = \sum_{i=1}^{n}\alpha_i K(x_i, x_j) + b. \tag{10}$$

In (10), $K(x_i,x_j)$ is the kernel function. The difference in $K(x_i,x_j)$ determines the performance of the regression model. This article uses the Gaussian kernel function as the choice of the regression model. The expression of the Gaussian kernel function is as follows:

$$K(x_i, x_j) = e^{-\frac{\|x_i - x_j\|^2}{\lambda}}. \tag{11}$$

In (11), λ is the kernel parameter.

The regression function form of WLSSVR can be obtained, and the Sunken principle is the most commonly used, and its specific expression is as follows:

$$f(x) = \sum_{i=1}^{n}\alpha_i^* K(x_i, x_j) + b \tag{12}$$

$$\sigma_i = \begin{cases} 1, & \left|\frac{\xi_i}{\hat{s}}\right| \le s_1 \\ (s_2 - \left|\frac{\xi_i}{\hat{s}}\right|)/(s_2 - s_1), & s_1 < \left|\frac{\xi_i}{\hat{s}}\right| \le s_2 \\ 10^{-4}, & \text{otherwize.} \end{cases} \tag{13}$$

In (13), s_1 and s_2 are determined by the distribution of sample error ξ_i, and $\hat{s}$ is related to the sample error ξ_i of WLSSVR

$$\hat{s} = \frac{Q}{2 \times 0.6745}. \tag{14}$$

In (14), Q is the interquartile difference of the sample error ξ_i.

B. Principle of WLSSVR Based on Entropy Method

The essence of WLSSVR is to weight according to the prediction error of the modeled samples. If the error is large, it means that the contribution of the sample to the model is small, the corresponding weight is small, and vice versa. However, the weights corresponding to different samples are linearly distributed, so there is a certain error in the selection of samples. According to the limitations of general WLSSVR, EM is used to optimize the regression model. When considering the weight relationship between different features, the EM can be used to judge the influence of the feature on the whole according to the degree of dispersion of each feature and determine its weight.

In the modeling problem, when the input variable x_i is an n-dimensional vector, i.e., $x_i = [x_{i1}, \ldots, x_{in}]$. Then, the data must be preprocessed first to eliminate the dimension and avoid the magnitude difference between the various features. Through the normalization method, the variables of each dimension fall

into the interval of [0,1], and the normalized data is

$$t_{ij} = \frac{A_{ij} - \min\{A_{ij}, A_{2j}, \ldots, A_{nj}\}}{\max\{A_{ij}, A_{2j}, \ldots, A_{nj}\} - \min\{A_{ij}, A_{2j}, \ldots, A_{nj}\}}. \tag{15}$$

Among them, $i = 12,3, \ldots$.n, and $j = 12,3, \ldots$.n.

It is supposed that input matrix A consists of n n-dimensional vectors

$$A = \begin{pmatrix} A_1 \\ A_2 \\ \vdots \\ A_n \end{pmatrix} = \begin{pmatrix} A_{11} & \cdots & A_{1n} \\ A_{21} & \cdots & A_{2n} \\ \vdots & \ldots & \vdots \\ A_{n1} & \cdots & A_{nn} \end{pmatrix}. \tag{16}$$

Therefore, the proportion of American characteristics of matrix A can be expressed as

$$B_{ij} = \frac{A_{ij}}{\sum_{i=1}^{n} A_{ij}}. \tag{17}$$

According to the definition of entropy, the input entropy value can be expressed by E_j

$$E_j = K_n \sum_{i=1}^{n} B_{ij} \cdot ln(B_{ij}). \tag{18}$$

Among them, the constant $K_n = -1/ln(\mathrm{n})$, so that $0 \le E_j \le 1$ can be guaranteed, and when $A_{1j} = A_{2j} = \cdots = A_{nj}$, $B_{1j} = B_{2j} = \cdots = B_{nj} = 1/\mathrm{n}$, so this time $E_j = 1$, the item has no reference significance, and the impact can be ignored.

Next, use D_j to indicate the degree of consistency of the jth dimension

$$D_j = 1 - E_j. \tag{19}$$

It can be seen from this that the greater the consistency, the smaller the entropy, and the better the system robustness, so the weight is greater, and vice versa, the weight w_j can be expressed as

$$w_j = \frac{D_j}{\sum_{i=1}^{n} D_j}, \quad j = 1, 2, \ldots, n. \tag{20}$$

Finally, new input variables with weights can be obtained

$$u_{ij} = t_{ij} \cdot w_j i = 1, 2, \ldots, n; j = 1, 2, \ldots, n. \tag{21}$$

It can be seen that the processed input data u_{ij} not only eliminates the influence of dimensions but also reflects the weight relationship between different features, which has a larger or smaller effect on modeling. The processed input and output data sample set $\{(x_i, y_i) \,|\, i = 12,\ldots,n,\}$ are applied to the WLSSVM modeling to build a regression model of the multi-input system

$$f(u) = \sum_{i=1}^{n} \alpha_i^* K(u, u_i) + b. \tag{22}$$

Fig. 4 shows the algorithm flow of the entropy method in WLSSVR.

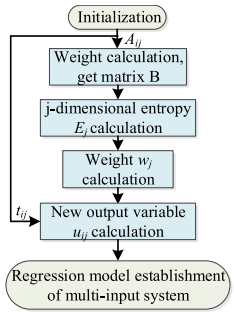

Fig. 4. Algorithm flow chart of the entropy method in WLSSVR.

IV. Application of the Improved COA

A. Basic Principle of Conventional COA

The Coyote optimization algorithm is an intelligent bionic optimization algorithm proposed by Juliano in 2018. Compared with other meta-heuristic algorithms. COA can improve the convergence efficiency while maintaining a high population diversity.

COA simulates the birth, growth, death, and migration of the coyote population. The specific process is as follows.

Step 1: Parameters N_p, N_c, D, are defined. Among them: N_p is the wolf group, N_c is the number of wolves without a group, D is the dimension of the search space.

Step 2: The coyotes are initialized, where the random individual wolf can be expressed as

$$x_{c,j}^{p,t} = lb_j + r_j(ub_j - lb_j). \tag{23}$$

Among them, $x_{c,j}^{p,t}$ can be described as: in the j dimension, the ith coyote individual in the p group at time t. ub_j and lb_j, respectively, represent the upper and lower limits of the jth dimension, and r_j is a random number in [0,1]. Therefore, the entire wolf pack can be expressed as

$$x_c^{p,t} = (x_{c,1}^{p,t}, x_{c,2}^{p,t}, x_{c,3}^{p,t}, \ldots, x_{c,D}^{p,t}). \tag{24}$$

Step 3: The habits of the wolf pack are defined. First of all, the coyote has certain adaptability, which is expressed by the function $fit_i^{p,t}$

$$fit_i^{p,t} = f(x_i^{p,t}). \tag{25}$$

In addition to adaptability, coyotes sometimes break away from or are expelled from the original group and form group changes. The probability of occurrence is defined as

$$P_e = 0.005 \cdot N_c^2, \quad N_c \le 14. \tag{26}$$

Step 4: There will be a chief wolf in every wolf pack. Since the chief wolf is the leader in its group, its ability to adapt to the environment is the worst. So, the chief wolf can be represented by $alpha^{p,t}$

$$alpha^{p,t} = \left\{ x_i^{p,t} \,\middle\|\, arg\,\{i = 1, 2, \ldots, N\} \min f(x_i^{pt}) \right\}. \tag{27}$$

In addition, there will be a cultural trend in the wolf pack, which can be expressed as

$$cult_j^{p,t} = \begin{cases} O^{p,t}_{(N_c+1)/2,j} & N_c \text{ is odd} \\ \frac{O^{p,t}_{(N_c+1)/2,j}+O^{p,t}_{N_c/2,j}}{2} & N_c \text{ is even} \end{cases}. \quad (28)$$

In (28), $O^{p,t}_{(N_c+1)/2,j}$ and $O^{p,t}_{N_c/2,j}$, respectively, represent the median of the j-dimension variable of all the coyotes in the p group at the tth time when N_c is odd or even.

Step 5: Coyotes will be born and die. And To simulate the genetic effect, the birth of a new coyote $pup_j^{p,t}$ is written as a combination of the social status of the parents and the environmental impact

$$pup_j^{p,t} = \begin{cases} soc^{p,t}_{m_1,j} & rand_j < P_s \text{ or } j = j_1 \\ soc^{p,t}_{m_2,j} & rand_j < P_s+P_a \text{ or } j = j_2 \\ R_j & \text{other} \end{cases}. \quad (29)$$

Among them, m_1 and m_2 are random coyotes from the p wolf pack, j_1 and j_2 are the two random dimensions of the problem, R_j and $rand_j$ are random numbers in [0,1] generated by uniform probability. And $P_s = \frac{1}{D}$, $P_a = \frac{1-P_s}{2}$.

Step 6: With the birth and death of wolves, new individuals will be produced. In addition, the new individual coyote is also affected by the wolves in the pack and cultural trends. The impact can be expressed by δ_1 and δ_2

$$\begin{cases} \delta_1 = alpha^{p,t} - x^{p,t}_{cr1} \\ \delta_2 = cult^{p,t} - x^{p,t}_{cr2}. \end{cases} \quad (30)$$

In (30), *cr1* and *cr2,* respectively, are random coyotes in the current population.

Affected by wolves and cultural trends within the group, all wolves in the group have been updated to obtain new_$x_i^{p,t}$, which can be expressed as

$$\text{new\_}x_i^{p,t} = x_i^{p,t} + r_1\delta_1 + r_2\delta_2. \quad (31)$$

Among them, r_1 and r_2 are real numbers in the range of [0,1] generated by uniform probability.

Due to the renewal of the wolf pack, it is necessary to select the best fit between the new coyotes and the original coyotes and to retain the best coyotes $x_i^{p,t+1}$

$$x_i^{p,t+1} = \begin{cases} \text{new\_}x_i^{p,t} & f(\text{new\_}x_i^{p,t}) < f(x_i^{p,t}) \\ x_i^{p,t} & \text{other} \end{cases}. \quad (32)$$

B. Principle of Improved COA

The disadvantage of conventional COA is that the birth of wolf cubs is determined randomly. So the lead wolf $alpha^{p,t}$ will often survive natural selection. Therefore, the general COA will not only appear in large useless numbers. Iteratively, it is easy to fall into the local optimum.

In (33), k is the number of iterations

$$\text{new\_}x_i^{p,t} = \omega_k \cdot x_i^{p,t} + r_1\delta_1 + r_2\delta_2 \quad (33)$$

where ω_k represents the state weight of the coyote. Therefore, if the number of iterations is small, the death of the little wolf will not have a big impact, and if the number of iterations is large, the older wolves in the population should also reduce their impact on the population. Therefore, ω_k can be expressed for

$$\omega_k = ln3^{(1+0.95k)^{\frac{1}{2k}}}. \quad (34)$$

When k is very small, $\omega_k \approx 1$ or even $\omega_k > 1$ happens, and new coyote individuals will not have a big impact on the entire optimization process. As k will gradually increase and ω_k will continue to decrease, new coyote individuals will gradually become dominant status. n was increased by introducing new coyote individuals.

Before introducing a new coyote individual, two operators need to be defined

$$\begin{cases} \delta_3 = cult^{p,t} - x^{p,t}_{cr3} \\ \delta_4 = cult^{p,t} - x^{p,t}_{cr4}. \end{cases} \quad (35)$$

In (35), $x^{p,t}_{cr3}$ and $x^{p,t}_{cr4}$ represent random coyotes in the group. On this basis, two parameters can be defined

$$\begin{cases} \bar{x}^t_{i,j} = \frac{x^{p,t}_{i,j}-lb_j}{ub_j-lb_j} \\ \bar{cult}^t_{i,j} = \frac{cult^{p,t}_{i,j}-lb_j}{ub_j-lb_j} \end{cases} \quad (36)$$

In (36), $\bar{x}^t_{i,j}$ and $\bar{cult}^t_{i,j}$, respectively, represent the level of the introduction of coyotes and the level of the current cultural trend of wolves.

Finally, the new individual coyote can be expressed as

$$\text{new\_}x_i^{p,t} = \begin{cases} \omega_k \cdot x_i^{p,t} + r_1\delta_1 + r_2\delta_2 & \bar{x}^t_{i,j} < 0 \\ \omega_k \cdot x_i^{p,t} + r_1\delta_1 + r_2\delta_2 + r_3\delta_3 & \bar{x}^t_{i,j} < \bar{cult}^t_{i,j} \\ \omega_k \cdot x_i^{p,t} + r_1\delta_1 + r_2\delta_2 + r_3\delta_3 + r_4\delta_4 & \bar{x}^t_{i,j} > \bar{cult}^t_{i,j}. \end{cases} \quad (37)$$

The r_1, r_2, r_3, r_4 are random numbers between [0,1]. In the new update formula, different operator values can be assigned according to the strength of different introduced wolves $\bar{x}^t_{i,j}$. If the newly introduced coyote is weak, then it will not have an impact on the wolf system. If $\bar{x}^t_{i,j}$ is strong enough, then it will have a great impact on the new wolf pack system. After that, the iteration rate of the lead wolf $alpha^{p,t}$ will be greatly improved, and the local optimal situation can be effectively reduced. Fig. 5 shows the algorithm flow chart of the improved COA.

V. Experimental Validation

A. Verification of EM-WLSSVR

The proposed EM-WLSSVR was compared with other algorithms, such as SVM and LSSVR to verify the usability and performance. Mean absolute error (MAE) and root-mean-square error (RMSE) methods are used to evaluate the modeling speed and accuracy of the model. And the expressions of MAE and RMSE are as follows:

$$\begin{cases} \text{MAE} = \max_{j=1}^{n} |y_j - y_{j0}| \\ \text{RMSE} = \sqrt{\frac{1}{n}\sum_{j=1}^{n}(y_j - y_{j0})^2} \end{cases}. \quad (38)$$

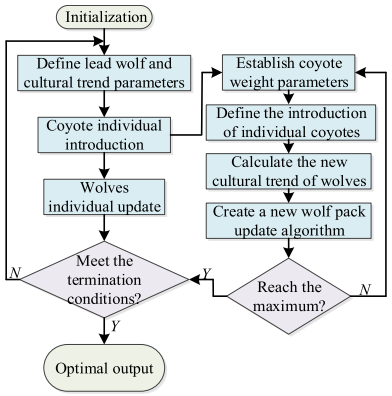

Fig. 5. Algorithm flow chart of entropy method in improved COA.

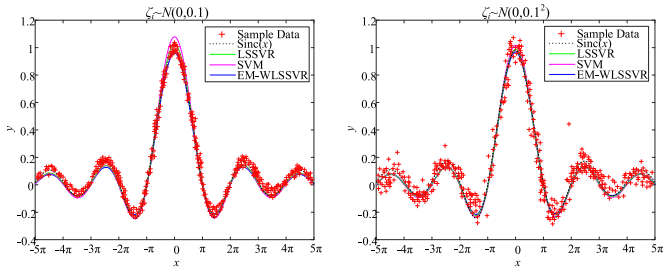

Fig. 6. Fitting results of SVM, LSSVR, and EM-WLSSVR under different SDs.

TABLE I
COMPARISON RESULTS OF MAE/RMSE OF DIFFERENT ALGORITHMS UNDER DIFFERENT STANDARD DEVIATIONS

SDs	SVM		LSSVR		EM-WLSSVR	
	MAE	RMSE	MAE	RMSE	MAE	RMSE
0.1	0.0894	0.0986	0.0692	0.0933	0.0378	0.0276
0.1^2	0.1269	0.1472	0.1031	0.1359	0.0722	0.0643

In (38), y_j is the output regression value and y_{j0} is the sample data.

First, the test *Sinc* function is used for performance testing. To effectively evaluate the performance of the algorithm, the training samples are contaminated by some noise. By giving 126 noisy training points and 252 test points without noise. The *Sinc* function can be expressed as:$10^{-4}\cdot$ s

$$y_i = \frac{\sin x_i}{x_i} + \xi_i, \quad x_i \sim U[-5\pi, 5\pi] \tag{39}$$

where ζ_i is noise, and $\xi_i \sim N(00.1)$.

Fig. 6 shows the one-time fitting results of SVM, LSSVR, and EM-WLSSVR under different SDs. EM-WLSSVR is the closest to the actual *Sinc* function compared to SVM and LSSVR. And when SDs are changed, EM-WLSSVR still has good performance. Table I records the average results of the three fitting methods in 15 independent runs of data sets with different SDs. The same result can be obtained from it.

To combine the torque model of EM-WLSSVR and SRM, first, obtain the training set $[i-\theta-T]$ through FEA, and optimize the hyperparameters with the help of improved COA. Then, the

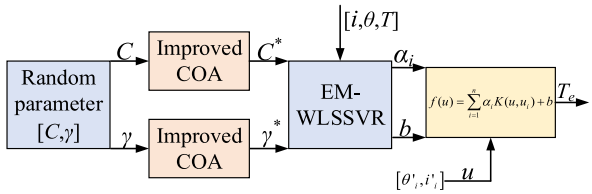

Fig. 7. Schematic diagram of EM-WLSSVR model based on improved COA for torque regression.

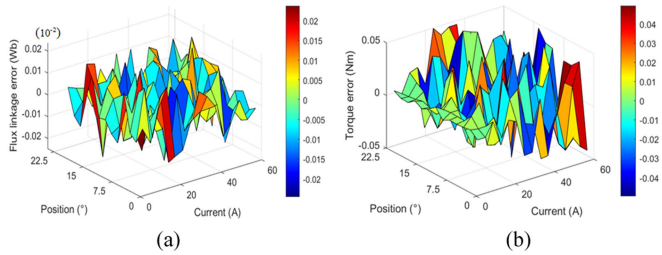

Fig. 8. Flux linkage and torque errors of EM-WLSSVR and FEA. (a) Flux linkage. (b) Torque.

TABLE II
TIME COMPARISON(OVERALL)

Methods	Flux linkage	Torque
	Time(s)	Time(s)
SVM	10.28	11.24
LSSVR	7.44	8.37
EM-WLSSVR	3.17	3.58

TABLE III
TIME COMPARISON(SINGLE)

Methods	Flux linkage	Torque
	Time(10^{-4} s)	Time(10^{-4} s)
SVM	3.44	3.75
LSSVR	2.46	2.81
EM-WLSSVR	1.08	1.19

regression parameters α_i and b of the EM-WLSSVR model. After training, input any i and θ to get the corresponding torque T_e. The schematic diagram is shown in Fig. 7. The same is true for the training process of the motor's flux linkage Ψ.

In simulation or experiment, the proposed nonlinear modeling method needs to select more robust parameters. In this respect, through the optimization and debugging of the algorithm, the parameters with good effect on nonlinear modeling are finally determined.

According to the EM-WLSSVR model regression method, a 3-D map of the flux linkage/torque errors concerning the rotor position θ and the phase current i is obtained, as shown in Fig. 8.

Table II shows the overall calculation time of SVM, LSSVR, and EM-WLSSVR. The calculation time of flux linkage/torque of EM-WLSSVR is 3.17 s/3.58 s, respectively. It is faster than SVM and LSSVR. Among them, the sampling interval of position is 0.1°, so 200 data points are in total. And the sampling interval of current is 0.2 A, so 200 data points in total. A total of

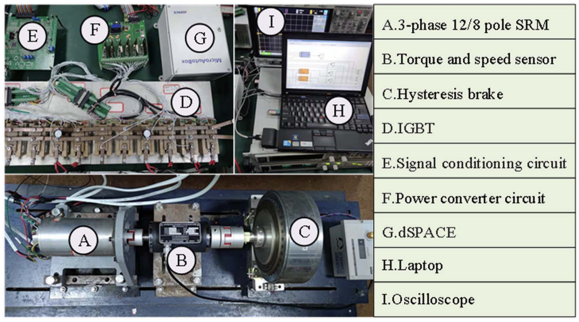

Fig. 9. Devices and platforms for testing dynamic characteristics.

TABLE IV
SRM EXPERIMENT PARAMETER TABLE

Parameter	SRM
Number of phases	3
Numbers of stator/rotor poles	12/8
Rated power(kW)	0.3
Reference speed (r/min)	3000
Rated voltage (V)	24
Resistance per phase (Ω)	0.22
Rough moment of inertia J_0 (kg·m^2)	0.0013
Rough damping coefficient F_0 (N·m·s)	0.02
Load Torque (Nm)	1
Turn-on angle (°)	-0.5
Turn-off angle (°)	20
Switching frequency (Hz)	400
Control frequency (Hz)	400

30 000 data points are needed to be calculated. Table III shows a comparison of sampling times for individual data points.

B Experimental Verification

The principle of the bench experiment is to insert the FEA data and the complete EM-WLSSVR algorithm into the Simulink model of the SRM to replace the original look-up table $[i-\theta-\Psi]$ and $[i-\theta-T]$. EM-WLSSVR adjusts the weight and kernel parameters of the algorithm according to the original discrete FEA data and obtains the corresponding Ψ and T according to i and θ at different times, which can achieve the function of real-time torque and flux linkage estimation. The experiment adopts direct torque control and torque sharing function control method as the basic closed-loop control strategy to verify the effectiveness of EM-WLSSVR in practical application. The original look-up tables $[i-\theta-\Psi]$ and $[i-\theta-T]$ used in the experiment are shown in Fig. 8.

Fig. 9 shows the experimental platform used for dynamic characteristics testing, including a 3-phase 12/8 SRM, a JN338 torque sensor with a torque range of 20 Nm, an FZ25J electromagnetic brake with a torque range of 25 Nm, a signal conditioning circuit, a power converter circuit, a dSPACE, IGBT, a laptop, and an oscilloscope. The Hall position sensor installed on the nonoutput shaft end of the motor inputs the detected position signal to dSPACE after passing the signal conditioning circuit, and so is the current signal. Table IV shows the specific experimental parameters of the 3-phase 12/8 SRM.

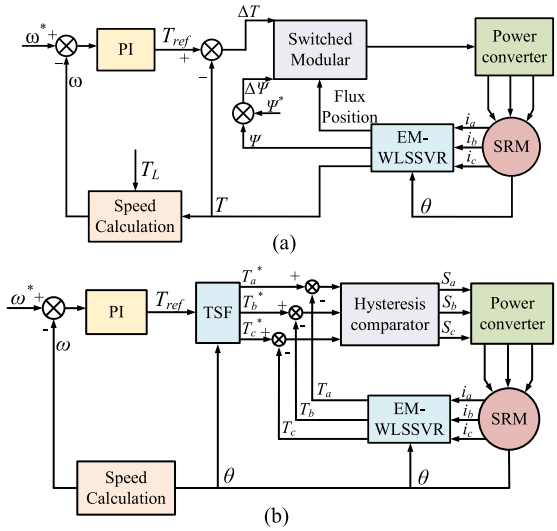

Fig. 10. Control block diagram. (a) DTC. (b) TSF.

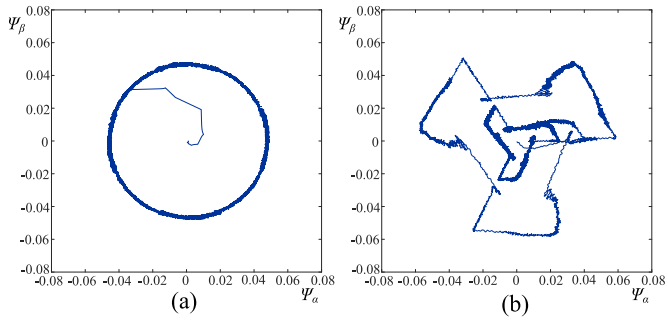

Fig. 11. Flux-linkage trajectories. (a) DTC. (b) TSF.

Fig. 10 shows the control block diagram of the most commonly used TSF and DTC in the SRM control method

$$\begin{cases} f_{\text{rise}}(\theta) = \frac{1}{2} - \frac{1}{2}\cos\frac{\pi}{\theta_{ov}}(\theta - \theta_{\text{on}}), \ \theta_{\text{on}} < \theta < \theta_{\text{on}} + \theta_{ov} \\ f_{\text{fall}}(\theta) = \frac{1}{2} + \frac{1}{2}\cos\frac{\pi}{\theta_{ov}}(\theta - \theta_{\text{off}}), \theta_{\text{off}} < \theta < \theta_{\text{off}} + \theta_{ov}. \end{cases} \tag{40}$$

Fig. 11 shows the flux linkage vector trajectory. The given reference flux linkage is 0.5 Wb-turns. The trajectory of the flux linkage of DTC is more circular, so the flux linkage is well controlled within the hysteresis bandwidth. The flux trajectory of TSF is symmetrical to the center, so it is more variable.

Figs. 12 and 13 show the current waveforms under the control of DTC and TSF. The two experiments are carried out under the working conditions of dc voltage 24 V, the reference current 22.5 A, and the speed setting of 1000 r/min. The results run by the EM-WLSSVR model agree well with the results run by measured data. It can be seen that no matter what kind of control method, EM-WLSSVR is in good agreement with the measured results and has high modeling precision.

Figs. 14 and 15 show the output waveform based on different modeling methods and different control methods. The experiments are all carried out under the conditions of reference

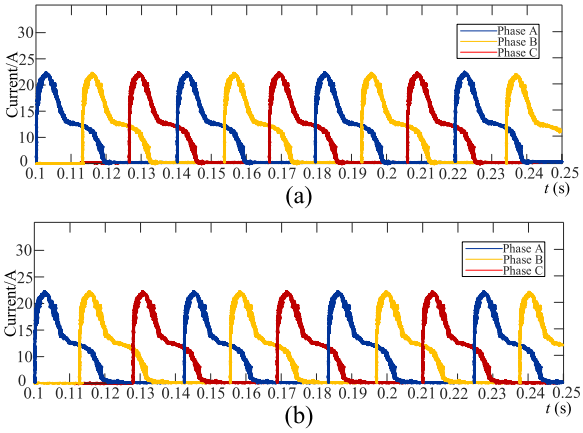

Fig. 12. Current waveform diagrams of different modeling methods under TSF. (a) EM-WLSSVR. (b) Look-up table.

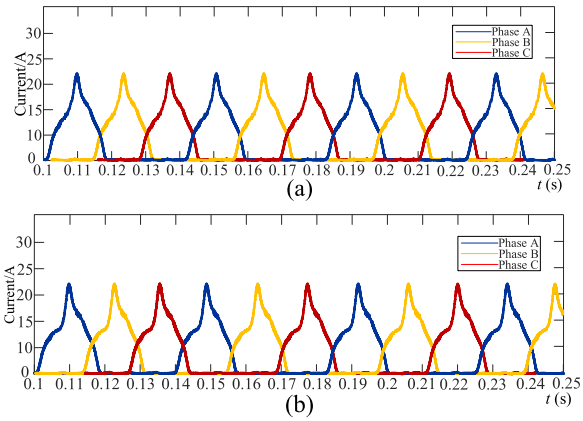

Fig. 13. Current waveform diagrams of different modeling methods under DTC. (a) EM-WLSSVR. (b) Look-up table.

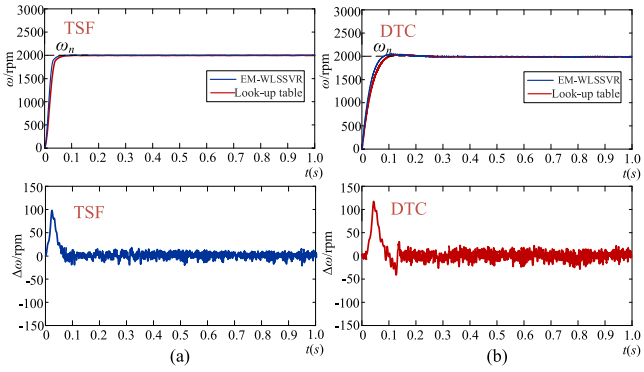

Fig. 14. EM-WLSSVR and look-up table static speed waveforms under different control methods. (a) TSF. (b) DTC.

speed 2000 r/min, and load torque T_L 0.4 Nm. And $\Delta\omega = \omega_{\text{EM-WLSSVR}}\text{-}\omega_{\text{table}}$, $\Delta T = T_{\text{EM-WLSSVR}}\text{-}T_{\text{table}}$.

In Fig. 14, it can be seen when the speed is in the rising range, EM-WLSSVR rises faster, which can prove that EM-WLSSVR has the characteristics of fast startup performance in

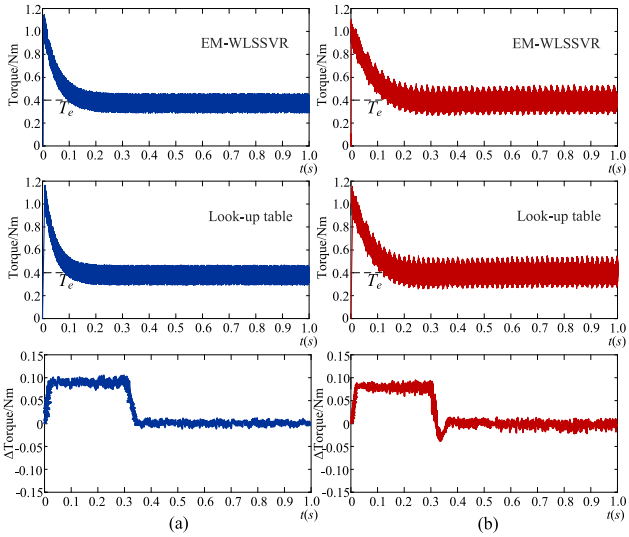

Fig. 15. EM-WLSSVR and look-up table static torque waveforms under different control methods. (a) TSF. (b) DTC.

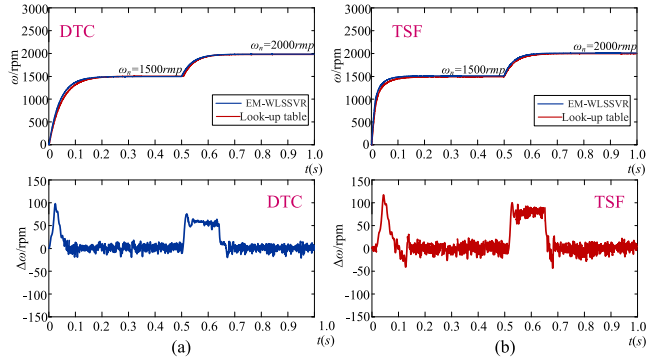

Fig. 16. Speed waveform of different control methods under dynamic speed conditions. (a) DTC. (b) TSF.

speed control. When the rotor speed is in steady state, the speed of EM-WLSSVR can better fit the speed of the look-up table.

Speed fluctuation and torque ripple is an important evaluation criterion for evaluating torque characteristics. It can be defined as

$$\begin{cases} \omega_R = \dfrac{\omega_m - \omega_{ref}}{\omega_{avg}} \times 100\% \\ T_{RM} = \dfrac{T_{\max} - T_{\min}}{T_{avg}} \times 100\% \end{cases}. \tag{41}$$

Fig. 15 shows the torque waveforms under different modeling methods and different control methods. According to (41), it can be calculated that the torque ripple T_{RM} brought by EM-WLSSVR and the look-up table.

Figs. 16 and 17 show the speed and torque waveforms of different control methods under dynamic speed conditions. The speed of EM-WLSSVR and look-up table are in good agreement. It can be seen that EM-WLSSVR has high modeling stability.

In Figs. 18 and 19, the load torque T_L increased from 0.4 Nm to 0.7 Nm at 0.4 s, and other experimental conditions were consistent with the steady-state experiment. Fig. 16 shows the output speed waveform in the dynamic experiment. It can be seen

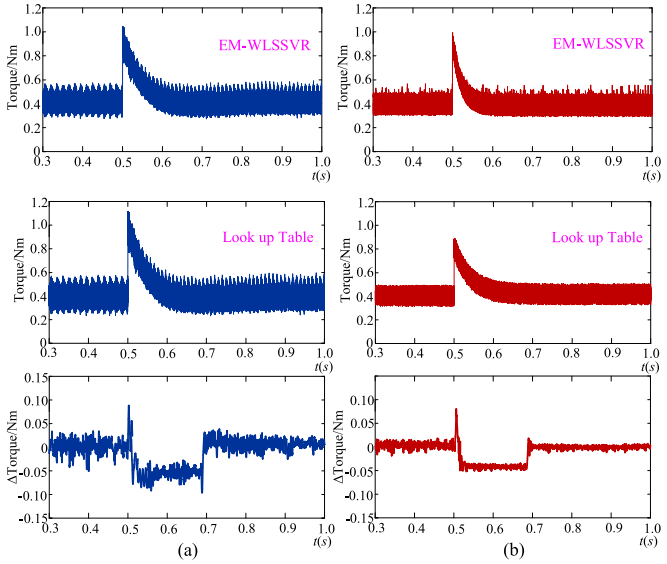

Fig. 17. Torque waveform of different control methods under dynamic speed conditions. (a) DTC. (b) TSF.

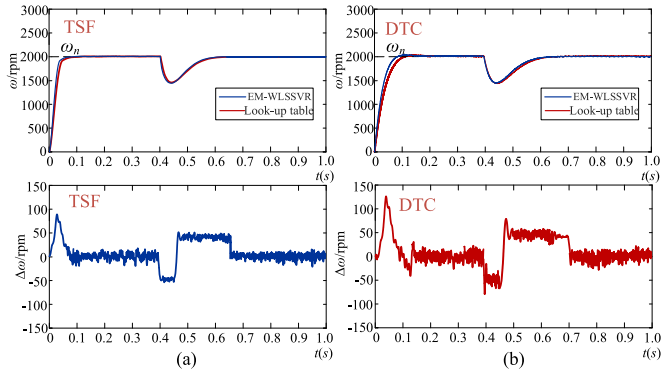

Fig. 18. EM-WLSSVR and look-up table dynamic speed waveforms under different control methods. (a) TSF. (b) DTC.

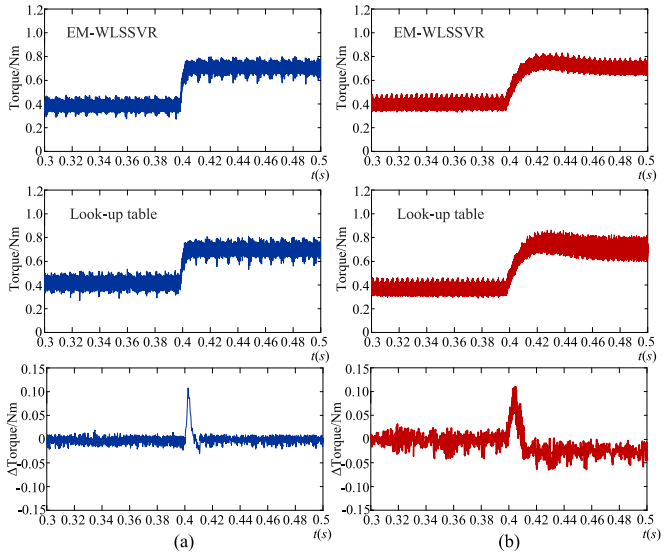

Fig. 19. EM-WLSSVR and look-up table dynamic torque waveforms under different control methods. (a) TSF. (b) DTC.

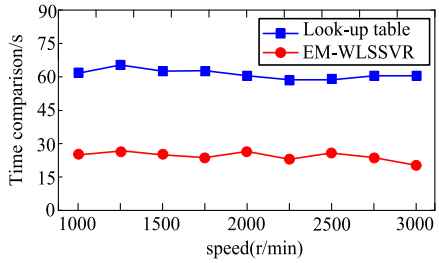

Fig. 20. Comparison of modeling times for different methods in experiments in the full speed range.

that compared with the look-up table, EM-WLSSVR improves the modeling speed on the premise of ensuring modeling accuracy. Fig. 17 shows the output speed waveform in the dynamic experiment. According to (41), it can be calculated that the torque ripple T_{RM} brought by EM-WLSSVR and the look-up table under TSF control are 48.46% and 49.69%, and 51.24% and 59.17% are brought by DTC. The results obtained by both TSF and DTC control methods are in good agreement with those obtained by look-up table method. It is worth noting that the reduction of torque ripple is independent of the proposed EM-WLSSVR.

Fig. 20 shows a comparison of the experimental modeling time for the look-up table and EM-WLSSVR in the full-speed range. It can be seen that EM-WLSSVR is about 35 s faster than the look-up table in the full speed range. This can prove that EM-WLSSVR can greatly speed up the time required for modeling under the premise of ensuring the modeling accuracy, which can effectively increase the experimental efficiency.

VI. Conclusion

In this article, an improved COA-based EM-WLSSVR modeling method is proposed for the modeling of SRM flux linkage and torque. This modeling method can improve the modeling speed on the premise of ensuring the modeling accuracy. The specific conclusions obtained in this article are as follows.

1) The experiment concluded that EM-WLSSVR tends to have higher data fitting accuracy and shorter modeling time.
2) The experiment concludes that the flux linkage trajectory of DTC is more circular, so the flux linkage is well controlled within the hysteresis bandwidth. The flux trajectory of the TSF is symmetric to the center and, therefore, varies widely.
3) The experimental conclusion: When EM-WLSSVR is used in static bench experiments, whether it is TSF control or DTC, the current, rotational speed, and torque waveforms obtained by EM-WLSSVR have little difference with the corresponding waveforms obtained by FEA.
4) The experimental conclusion: When EM-WLSSVR is used in dynamic bench experiments, whether it is TSF or DTC, EM-WLSSVR has high tracking and stability in dynamic experiments.

The modeling method proposed in this study is mainly implemented based on the machine learning method. When the

system parameters are changed, the machine learning algorithm needs to be retrained. Compared with the look-up table method, the nonlinear model established by EM-WLSSVR also behaves better. However, some regression parameters need to be adjusted, which will increase the complexity of the model. In future research, this study will consider the impact of system interference on the training algorithm, the influence of control parameters on the robustness of the system under multiple working conditions, as well as the further combination of the training algorithm and SRM, such as the combination with the power converter.

REFERENCES

[1] X. Tian, Y. Cai, X. Sun, Z. Zhu, and Y. Xu, "A novel energy management strategy for plug-in hybrid electric buses based on model predictive control and estimation of distribution algorithm," *IEEE/ASME Trans. Mechatro.*, vol. 27, no. 6, pp. 4350–4361, Dec. 2022.

[2] F. Yu, W. Zhang, Y. Shen, and J. Mao, "A nine-phase permanent magnet electric-drive-reconstructed onboard charger for electric vehicle," *IEEE Trans. Energy Convers.*, vol. 33, no. 4, pp. 2091–2101, Dec. 2018.

[3] X. Sun, Y. Xiong, M. Yao, X. Tang, and X. Tian, "A unified control method combined with improved TSF and LADRC for SRM using modified grey wolf optimization algorithm," *ISA Trans.*, vol. 131, pp. 662–671, Dec. 2022.

[4] Z. Shi, X. Sun, G. Lei, X. Tian, Y. Guo, and J. Zhu, "Multiobjective optimization of a five-phase bearingless permanent magnet motor considering winding area," *IEEE/ASME Trans. Mechatro.*, vol. 27, no. 5, pp. 2657–2666, Oct. 2022.

[5] X. Sun, Y. Zhang, Y. Cai, and X. Tian, "Compensated deadbeat predictive current control considering disturbance and VSI nonlinearity for in-wheel PMSM," *IEEE/ASME Trans. Mechatro.*, vol. 27, no. 5, pp. 3536–3547, Oct. 2022.

[6] X. Sun, N. Xu, and M. Yao, "Sequential subspace optimization design of a dual three-phase permanent magnet synchronous hub motor based on NSGA III," *IEEE Trans. Transport. Electrific.*, vol. 9, no. 1, pp. 622–630, Mar. 2023.

[7] F. J. Perez-Cebolla, A. Martinez-Iturbe, B. Martín-del-Brío, C. Bernal, and A. Bono-Nuez, "Nonlinear lumped-circuit model for switched reluctance motors exhibiting core losses," *IEEE Trans. Ind. Electron.*, vol. 63, no. 6, pp. 3433–3445, Jun. 2016.

[8] N. R. Patel, V. A. Shah, and M. M. Lokhande, "A novel approach to the design and development of 12/15 radial field C-core switched reluctance motor for implementation in electric vehicle application," *IEEE Trans. Veh. Technol.*, vol. 67, no. 9, pp. 8031–8040, Jan. 2018.

[9] D. Xiao, J. Ye, G. Fang, Z. Xia, X. Wang, and A. Emadi, "Improved feature-position-based sensorless control scheme for SRM drives based on nonlinear state observer at medium and high speeds," *IEEE Trans. Power Electron.*, vol. 36, no. 5, pp. 5711–5723, May 2021.

[10] S. Song, L. Ge, and M. Zhang, "Data-reconstruction-based modeling of SRM with few flux-linkage samples from torque-balanced measurement," *IEEE Trans. Energy Convers.*, vol. 31, no. 2, pp. 424–435, Jun. 2016.

[11] X. Sun, Y. Xiong, M. Yao, and J. Wu, "High fault-tolerance evaluation on position signal for switched reluctance motor drives," *IEEE Trans. Energy Convers.*, vol. 37, no. 3, pp. 1844–1853, Sep. 2022.

[12] J. B. Bartolo, M. Degano, J. Espina, and C. Gerada, "Design and initial testing of a high-speed 45-kW switched reluctance drive for aerospace application," *IEEE Trans. Ind. Electron.*, vol. 64, no. 2, pp. 988–997, Feb. 2017.

[13] L. Feng, X. Sun, X. Tian, and K. Diao, "Direct torque control with variable flux for an SRM based on hybrid optimization algorithm," *IEEE Trans. Power Electron.*, vol. 37, no. 6, pp. 6688–6697, Jun. 2022.

[14] X. Sun, Y. Xiong, M. Yao, and X. Tang, "A hybrid control strategy for multimode switched reluctance motors," *IEEE/ASME Trans. Mechatro.*, vol. 27, no. 6, pp. 5605–5614, Dec. 2022.

[15] J. Dong et al., "Advanced dynamic modeling of three-phase mutually coupled switched reluctance machine," *IEEE Trans. Energy Convers.*, vol. 33, no. 1, pp. 146–154, Mar. 2018.

[16] C. Lin, W. Wang, M. McDonough, and B. Fahimi, "An extended field reconstruction method for modeling of switched reluctance machines," *IEEE Trans. Magn.*, vol. 48, no. 2, pp. 1051–1054, Feb. 2012.

[17] O. Safdarzadeh, A. Mahmoudi, E. Afjei, and H. Torkaman, "Rotary-linear switched reluctance motor: Analytical and finite-element modeling," *IEEE Trans. Magn.*, vol. 55, no. 5, May 2019, Art. no. 8200710.

[18] F. Perez and A. Martinez, "Nonlinear lumped-circuit model for switched reluctance motors exhibiting core losses," *IEEE Trans. Ind. Electron.*, vol. 63, no. 6, pp. 3433–3445, Jun. 2016.

[19] X. Sun, K. Diao, G. Lei, Y. Guo, and J. Zhu, "Direct torque control based on a fast modeling method for a segmented-rotor switched reluctance motor in HEV application," *IEEE J. Emerg. Sel. Topics Power Electron.*, vol. 9, no. 1, pp. 232–241, Feb. 2021.

[20] Y. Cai, Y. Wang, H. Xu, S. Sun, C. Wang, and L. Sun, "Research on rotor position model for switched reluctance motor using neural network," *IEEE/ASME Trans. Mechatro.*, vol. 23, no. 6, pp. 2762–2773, Dec. 2018.

[21] W. Ding and D. Liang, "Modeling of a 6/4 switched reluctance motor using adaptive neural fuzzy inference system," *IEEE Trans. Magn.*, vol. 44, no. 7, pp. 1796–1804, Jan. 2008.

[22] A. Wang, L. Liu, J. Qiu, and G. Feng, "Event-triggered robust adaptive fuzzy control for a class of nonlinear systems," *IEEE Trans. Fuzzy Syst.*, vol. 27, no. 8, pp. 1648–1658, Aug. 2019.

[23] J. Cai, Z. Q. Deng, R. Y. Qi, Z. Y. Liu, and Y. H. Cai, "A novel BVC-RBF neural network based system simulation model for switched reluctance motor," *IEEE Trans. Magn.*, vol. 47, no. 4, pp. 830–838, Apr. 2011.

[24] J. Cai, Y. Tang, G. Yang, Y. Yan, and X. Zhang, "A backpropagation multidimensional Taylor network model for measured 3-D data fitting," *IEEE Trans. Instrum. Meas.*, vol. 72, 2023, Art. no. 2526910.

[25] P. Zhou, D. Guo, H. Wang, and T. Chai, "Data-driven robust M-LS-SVR-based NARX modeling for estimation and control of molten iron quality indices in blast furnace ironmaking," *IEEE Trans. Neural. Netw. Learn. Syst.*, vol. 29, no. 9, pp. 4007–4021, Sep. 2018.

[26] H. Chen, H. Qiao, L. Xu, Q. Feng, and K. Cai, "A fuzzy optimization strategy for the implementation of RBF LSSVR model in Vis–NIR analysis of pomelo maturity," *IEEE Trans. Ind. Inform.*, vol. 15, no. 11, pp. 5971–5979, Nov. 2019.

[27] H. Chen, W. Yan, L. Chen, M. Sun, and Z. Liu, "Analytical polynomial models of nonlinear magnetic flux linkage for SRM," *IEEE Trans. Appl. Supercond.*, vol. 28, no. 3, Apr. 2018, Art. no. 5205307.

[28] D. S. Mihic, M. V. Terzic, and S. N. Vukosavic, "A new nonlinear analytical model of the SRM with included multiphase coupling," *IEEE Trans. Energy Convers.*, vol. 32, no. 4, pp. 1322–1334, Dec. 2017.

[29] J. Gao, L. Dai, and W. Zhang, "Improved genetic optimization algorithm with subdomain model for multi-objective optimal design of SPMSM," *CES Trans. Elect. Machines Syst.*, vol. 2, no. 1, pp. 160–165, Mar. 2018.

[30] J. H. Lee, J. Kim, J. Song, D. Kim, Y. Kim, and S. Jung, "Distance-based intelligent particle swarm optimization for optimal design of permanent magnet synchronous machine," *IEEE Trans. Magn.*, vol. 53, no. 6, Jun. 2017, Art. no. 7206804.

[31] X. Sun, Z. Jin, M. Xue, and X. Tian, "Adaptive ECMS with gear shift control by grey wolf optimization algorithm and neural network for plug-in hybrid electric buses," *IEEE Trans. Ind. Electron.*, vol. 71, no. 1, pp. 667–677, Jan. 2024.

[32] Chen, J. Y. and J. Liang, "Recursive robust least squares support vect X. or regression based on maximum correntropy criterion," *Neurocomputing*, vol. 97, no. 15, pp. 63–73, Nov. 2012.

[33] X. Sun, Y. Zhang, X. Tian, J. Cao, and J. Zhu, "Speed sensorless control for IPMSMs using a modified MRAS with gray wolf optimization algorithm," *IEEE Trans. Transp. Electrific.*, vol. 8, no. 1, pp. 1326–1337, Mar. 2022.

[34] J. Kim and R. Kim, "Sensorless direct torque control using the inductance inflection point for a switched reluctance motor," *IEEE Trans. Ind Electron.*, vol. 65, no. 12, pp. 9336–9345, Dec. 2018.

[35] L. Feng, X. Sun, D. Guo, M. Yao, and K. Diao, "Advanced torque sharing function strategy with sliding mode control for switched reluctance motors," *IEEE Trans. Transp. Electrific.*, to be published, doi: 10.1109/TTE.2023.3287159.

[36] M. H. Holakooie, M. Ojaghi, and A. Taheri, "Modified DTC of a six-phase induction motor with a second-order sliding-mode MRAS-based speed estimator," *IEEE Trans. Power Electron.*, vol. 34, no. 1, pp. 600–611, Jan. 2019.

[37] S. Song, R. Hei, R. Ma, and W. Liu, "Model predictive control of switched reluctance starter/generator with torque sharing and compensation," *IEEE Trans. Transp. Electrific.*, vol. 6, no. 4, pp. 1519–1527, Dec. 2020.

[38] Q. Sun, J. Wu, C. Gan, M. Shen, and Y. Hu, "Investigation of direct torque control and torque sharing function strategy for switched reluctance motor applications," in *Proc. 18th Int. Conf. Elect. Machines Syst.*, 2015, pp. 864–868.

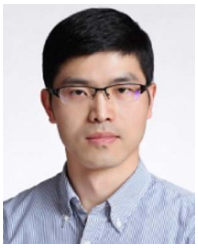

Xiaodong Sun (Senior Member, IEEE) received the B.Sc. degree in electrical engineering and the M.Sc. and Ph.D. degrees in control engineering from Jiangsu University, Zhenjiang, China, in 2004, 2008, and 2011, respectively.

Since 2004, he has been with Jiangsu University, where he is currently a Professor in Vehicle Engineering with the Automotive Engineering Research Institute. From 2014 to 2015, he was a Visiting Professor with the School of Electrical, Mechanical, and Mechatronic Systems, University of Technology Sydney, Sydney, Australia. He has authored or coauthored more than 100 refereed technical papers and one book, and he is the holder of 42 patents in his areas of interest. His current teaching and research interests include electrified vehicles, electrical machines, electrical drives, and energy management.

Dr. Sun is an Associate Editor for IEEE TRANSACTIONS ON INDUSTRIAL ELECTRONICS, IEEE TRANSACTIONS ON TRANSPORTATION ELECTRIFICATION, and an Editor of IEEE TRANSACTIONS ON ENERGY CONVERSION.

Nuonuo Wang was born in Lianyungang, China, in 2000. He received the B.S. degree in vehicle engineering in 2022 from Jiangsu University, Zhenjiang, China, where he is currently working toward the M.S. degree in vehicle engineering.

His current research interests include position sensorless control and control strategy optimization of switched reluctance motors for electric vehicle propulsion.

Yunfei Cao was born in Suzhou, China, in 1998. He received the B.S. degree in vehicle engineering in 2021 from Jiangsu University, Zhenjiang, China, where he is currently working toward the M.S. degree in vehicle engineering.

His current research interests include hybrid electric vehicles, optimal energy control strategy, and control strategy optimization of switched reluctance motors for electric vehicle propulsion.

Dong Guo received the B.Sc. and M.Sc. degrees from the Chongqing University of Technology, Chongqing, China, in 2007 and 2010, respectively, and the Ph.D. degree from the Southwest Jiaotong University, Chengdu, China, in 2015, all in mechanical engineering.

Since 2015, he has been with Chongqing University of Technology, where he is currently a Professor in Vehicle Engineering and he is the Deputy Dean with the School of Vehicle Engineering. He has authored or coauthored more than 40 refereed technical papers and one book, and his is the holder of 16 patents and 8 software works in his areas of interest. His current teaching and research interests include electric drive systems, intelligent cockpit systems, and NVH test and analysis of driveline systems.

Dr. Guo was the recipient of the China Machinery Industry Science and Technology Award, the Chongqing Science and Technology Award, and the China Automotive Engineering Society Science and Technology Award.

Ming Yao received the B.S. degree in vehicle engineering and the M.Sc. and Ph.D. degrees in vehicle operation engineering from Jiangsu University, Zhenjiang, China, in 2000, 2006, and 2019, respectively.

He is currently an Associate Professor with the School of Automotive and Traffic Engineering, Jiangsu University. His main research interests include electrified vehicles, vehicles' safety technology and energy saving, and environmental protection technology of vehicles.

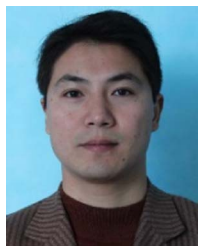

Yueping Sun was born in Changzhou, China, in 1982. He received the B.Sc. degree in electronic information engineering, and the M.Sc. and Ph.D. degrees in detection technology and automatic equipment from Jiangsu University, Zhenjiang, China, in 2004, 2007, and 2016, respectively.

Since 2004, he has been with Jiangsu University, where he is currently a Lecturer with the School of Electrical and Information Engineering. His current research interests include motor drives, motor movement control, hybrid electric vehicles, and intelligent control.

Yefei Xiong was born in Nanjing, China, in 1998. He received the B.S. degree in vehicle engineering in 2020 from Jiangsu University, Zhenjiang, China, where he is currently working toward the M.Sc. degree.

His current research interests include modeling, structure designing, and controlling of switched reluctance motors for electric vehicle propulsion.